The Rotation-disk Connection in Young Brown Dwarfs: Strong Evidence for Early Rotational Braking

Keavin Moore[1,2], Aleks Scholz[3] , and Ray Jayawardhana[1,4]
[1] Faculty of Science, York University, 4700 Keele Street, Toronto, ON M3J 1P3, Canada; keavin.moore@gmail.com
[2] Department of Earth and Planetary Sciences, McGill University, 3450 rue University, Montréal, QC H3A 0E8, Canada
[3] SUPA, School of Physics and Astronomy, University of St. Andrews, North Haugh, St. Andrews, KY16 9SS, UK
[4] Department of Astronomy, Cornell University, Ithaca, NY 14853, USA

Abstract

We use *Kepler*/*K2* light curves to measure rotation periods of brown dwarfs and very low mass stars in the Upper Scorpius star-forming region. Our sample comprises a total of 104 periods. Depending on the assumed age of Upper Scorpius, about a third of them are for brown dwarfs. The median period is 1.28 day for the full sample and 0.84 day for the probable brown dwarfs. With this period sample, we find compelling evidence for early rotational braking in brown dwarfs, caused by the interaction between the central object and the disk. The median period for objects with disks is at least 50% longer than for those without. Two brown dwarfs show direct signs of "disk-locking" in their light curves, in the form of dips that recur on a timescale similar to the rotation period. Comparing the period samples for brown dwarfs at different ages, there is a clear need to include rotational braking into period evolution tracks between 1 and 10 Myr. A locked period over several Myr followed by spin-up due to contraction fits the observational data. We conclude that young brown dwarfs are affected by the same rotational regulation as stars, though they start off with significantly faster rotation, presumably set by initial conditions.

Key words: accretion, accretion disks – brown dwarfs – stars: formation – stars: rotation

1. Introduction

Low mass stars lose angular momentum over the course of their life, through rotational braking via the star-disk interaction in the first few Myr and via magnetically driven stellar winds on longer timescales (Herbst et al. 2007). How effective these processes are in objects with ultra-low masses, i.e., brown dwarfs and free-floating planets, remains an open question that is the subject of active research (Schwarz et al. 2016; Zhou et al. 2016; Vasconcelos & Bouvier 2017; Bryan et al. 2018). There is a consensus, however, that brown dwarfs rotate faster than solar-mass stars at all ages (see review by Bouvier et al. 2014, and references therein). For very young brown dwarfs, rotation periods are in the range of 1–3 days (Scholz & Eislöffel 2004a; Mohanty et al. 2005), whereas evolved brown dwarfs spin with periods of a few hours up to a day (Zapatero Osorio et al. 2006; Reiners & Basri 2008; Metchev et al. 2015).

The ideal way to assess rotation rates for large samples is measuring periods from photometric light curves. Through rotation, surface features like magnetic spots or dusty clouds will modulate the brightness, with a period corresponding to the rotation period. Measuring rotation periods for objects with a range of ages is the fundament for analyzing the evolution of angular momentum in the substellar regime. First periods for brown dwarfs ($M < 0.08\,M_\odot$) in star-forming regions and open clusters have been derived from ground-based wide-field data over the past 15 or so years, including σ Orionis (Caballero et al. 2004; Scholz & Eislöffel 2004a; Cody & Hillenbrand 2010), Chamaeleon-I (Joergens et al. 2003; Cody & Hillenbrand 2014), NGC 2264 (Lamm et al. 2005), and ONC (Rodríguez-Ledesma et al. 2009). In addition, targeted observations of individual field brown dwarfs have yielded substantial period samples (e.g., Bailer-Jones & Mundt 2001; Harding et al. 2013; Metchev et al. 2015; Miles-Páez et al. 2017). For brown dwarfs with

typical periods around a day and small photometric amplitudes, ground-based monitoring—with daytime gaps and red noise caused by atmospheric effects—remains a challenging proposition.

The failing of the reaction wheels on the *Kepler* satellite and its ensuing "second" mission *K2* was a blessing in disguise for work on stellar and substellar rotational evolution. During its *K2* incarnation, the spacecraft has been able to observe numerous young clusters near the ecliptic with unprecedented cadence and precision (Howell et al. 2014), allowing us to revisit the issue of brown dwarf rotation with significantly improved data. This paper is the third in a series aiming to establish robust period samples for well-characterized samples of brown dwarfs, using *K2* light curves.

In the first paper, we published the first periods for a (small) sample of brown dwarfs in the ∼10 Myr old Upper Scorpius region (Scholz et al. 2015), suggesting that disk locking is inefficient in the substellar regime. In the second paper, we used multiple period search techniques to establish periods for 18 spectroscopically confirmed Taurus brown dwarfs (Scholz et al. 2018). We found a link between the presence of disks (detected via Spitzer infrared excess) and slow rotation, thus evidence for rotational braking by the disks. Moreover, when extrapolated to the age of the solar system, the periods of young brown dwarfs fit the spin-mass trend of solar system planets, demonstrating the link between planetary, substellar, and stellar rotation.

In this paper we return to Upper Scorpius, now making use of the full sample of brown dwarfs covered in *K2* campaigns 2 and 15, as well as the improved systematics correction compared to 2015. The main purpose of this paper is to examine the rotational regulation in brown dwarfs by disks with the enlarged sample and improved methodology. Broadly speaking, there are three different ways of testing the link between rotation and disks: (a) comparing period distributions

for objects with and without disks, identified by excess mid-infrared emission (Rebull et al. 2006), (b) finding objects with direct evidence for a disk feature (e.g., a warp) that is corotating with the surface (Stauffer et al. 2015), and (c) comparing rotation rates at different ages to test for rotational braking. In analyzing our new period sample in Upper Sco, we find that all three approaches consistently yield evidence for rotational regulation by disks.

2. The Sample

The Upper Scorpius star-forming region has been observed twice during the course of the *Kepler*/*K2* mission (Howell et al. 2014). Campaign 2 lasted 82 days, from 2014 August 23 to 2014 November 13, while Campaign 15 occurred over 89 days, from 2017 August 23 to 2017 November 20.

Our sample of brown dwarfs and very low mass stars was constructed as follows. We start with the 52 objects examined in Scholz et al. (2015). This sample has been selected using multi-band photometry and proper motions by Dawson et al. (2013). Spectroscopic follow-up has shown that the over-whelming majority of these sources are mid to late M dwarfs with evidence of youth (Dawson et al. 2014). We select 9 more objects observed in Campaign 2, and 8 from Campaign 15, found by cross-matching the membership list by Cook et al. (2017) (more precisely, their L-ZYJHK and C-ZYJHK HK-cut samples) and the full list of *K2* targets in those campaigns. Thus, our primary sample in the current paper comprises a total of 69 objects, the majority of which have been confirmed spectroscopically (see Table 1). We refer to this primary sample as "sample A."

Sample A only includes objects from a fraction of the entire Upper Sco association. Rebull et al. (2018) have recently compiled a list of likely members based on photometry and proper motions for a much larger region. We supplement our object list by selecting a subsample from Rebull et al. (2018) using a magnitude cutoff $J > 12.5$ and a color cutoff $J - K < 2$. These cutoffs are defined based on our sample A and select objects with little extinction and masses near or below the substellar boundary (see Figure 1). We also largely avoid the area of the sky including the much younger star-forming region ρ Oph ($246.14 <$ R.A. < 247.43, $-25.19 <$ decl. < -24) to prevent contamination from this region. This step gives us 135 more objects, which we refer to as "sample B." In total, our A and B samples contain 204 objects. Because of their different selection criteria, we keep these two samples separate for the analysis in this section, but we find that in terms of their rotational properties there is no significant difference.

Figure 1 is a color–magnitude diagram, displaying J versus $J - K$ for samples A (black) and B (cyan). This figure includes all objects from Rebull et al. (2018) as blue star symbols (excluding the ρ Oph region), with 5, 10, and 15 Myr isochrones from Baraffe et al. (2015) overplotted. The adopted cutoff of $J > 12.5$ is shown as the dashed black line, and our A and B samples are displayed below this cutoff. Approximate mass limits are indicated, based on J magnitudes from the 10 Myr isochrone of Baraffe et al. (2015). Assuming an average distance of 145 pc (Cook et al. 2017), the substellar limit ($0.08 M_\odot$) in Upper Sco should be between $J = 12.8$ for an age of 5 Myr and 13.5 for an age of 10 Myr. Our selection should safely encompass all substellar objects, but will also include a number of very low mass stars with masses above the substellar limit.

3. *K2* Light curves and Period Search

3.1. K2 *Light curves*

The main purpose of this study is the search for light curves with periodic sinusoidal variations, which can be interpreted as rotation periods caused by surface spots on the targets. We use the high-level science product K2SFF reduced light curves (based on an algorithm from Vanderburg & Johnson 2014) from the *K2* MAST archive for investigation of periodicity, for both campaign 2 and campaign 15. *K2* light curves suffer from systematics due to spacecraft drift, and a number of algorithms have been developed to correct for that, K2SFF being one. The suitability of K2SFF light curves to recover periodic signals in comparison with other algorithms has been demonstrated by, for example, Esselstein et al. (2018) and also in our own previous study (Scholz et al. 2018). In agreement with the literature (see, for example, Rebull et al. 2018) we find by visual inspection that light curves from different algorithms generally give consistent results when searching for coherent periods that are stable over many cycles (as expected for our targets).

The light curves for the 69 (sample A) plus 135 (sample B) targets were first examined by eye. Many have obvious periods throughout the observations. There is a clear "jump" present in many light curves around the middle of the campaign; this step function between the first and second halves of the campaign has been noted before as an artifact of the K2SFF reduction process (e.g., Hedges et al. 2018), as the light curve is detrended in separate "stability regimes" to avoid the reorientation of the spacecraft. Many of our light curves also show a large spike in flux near the middle of the campaign. The pixel data identify these events as either "argabrightening," in which all pixels are equally illuminated, or "cosmic ray in collateral data." It appears that Mars crosses the frame during this time in the campaign, adding flux across all pixels of the CCD, resulting in an artifact after K2SFF reduction. Therefore, any anomalies occurring around this time are discarded.

3.2. *Period Search*

We calculated the autocorrelation function (ACF) of all 204 light curves to measure periods. The ACF, as the name suggests, tests the correlation of a light curve with itself, shifting the copy by a time delay δ. The ACF will then show a peak at $\delta = 0$, as expected, and any additional peaks at $\delta = N \times P$ reveal an underlying period, if one is present, allowing its extraction. The ACF is insensitive to the shape of the periodic signal and robust against changes in amplitude. It has been widely adopted as one of the main period search methods in studies using *Kepler* and *K2* data (McQuillan et al. 2013; Aigrain et al. 2015; Stelzer et al. 2016; Giles et al. 2017).

Our procedure was analogous to that of Scholz et al. (2018), computing the ACF first for the entire light curve, and then independently for seven equal segments of the light curve. A period was accepted if present in at least two of seven segments within a tolerance of 0.1 day, and if it could be visually confirmed by eye. The standard deviation over the segments with a consistent period gives us an estimate for the error of the period. The few ACF periods that could not be convincingly visually confirmed in their corresponding segments, even if appearing in multiple segments, had only weak maxima in their ACF. As a final step, we phase-fold a segment of the light curve. These phase plots are shown in the Appendix. For

Table 1
Our Catalog of Objects with Periods in Sample A, Including their Spectral Type, Where Available

EPIC	R.A. (J2000)	Decl. (J2000)	SpT	P_{ACF} (d)	N	ΔP (d)	Proposal ID
K2 GO2010							
202632400	16 17 56.087	−28 56 39.97	⋯	1.38	3	0.05	GO2010
203083616	16 14 52.534	−27 18 55.71	⋯	0.65	6	0.01	GO2010
203348744	16 03 02.358	−26 26 16.37	⋯	4.29	3	0.02	GO2010
203420271	16 03 37.991	−26 11 54.43	⋯	1.28	7	0.04	GO2010
203544427	15 55 42.290	−25 46 47.79	⋯	1.12	6	0.03	GO2010
204078097	16 09 58.525	−23 45 18.61	M6.5[a]	1.41	6	0.09	GO2010
204099713	16 11 26.300	−23 40 05.97	M5.5[b]	1.77	5	0.03	GO2010
204126288	16 16 45.394	−23 33 41.39	M5.0[b]	0.21	7	0.01	GO2010
204149252	16 13 34.766	−23 28 15.61	M5.75[c]	0.97	7	0.04	GO2010
204202443	16 15 28.195	−23 15 43.95	M5.5[c]	1.03	5	0.03	GO2010
204204414	16 15 36.479	−23 15 17.52	M5.75[c]	0.61	7	0.01	GO2010
204239143	16 11 38.375	−23 07 07.27	M6.25[c]	0.71	7	0.03	GO2010
204344180	16 14 32.870	−22 42 13.35	M6.5[b]	1.76	6	0.04	GO2010
204367193	16 11 54.395	−22 36 49.19	M6.25[c]	0.48	7	0.01	GO2010
204393705	16 13 26.656	−22 30 34.84	M6.25[c]	1.48	7	0.02	GO2010
204418005	16 09 04.514	−22 24 52.39	M7.0[b]	0.54	6	0.03	GO2010
204439854	16 11 34.703	−22 19 44.21	M5.75[c]	0.60	4	0.02	GO2010
204451272	16 08 22.294	−22 17 02.90	M5.75[c]	0.96	6	0.01	GO2010
204555809	16 09 01.976	−21 51 22.54		0.27	7	0.01	GO2010
K2 C02							
202795175	16 23 41.870	−28 20 12.70	⋯	0.83	6	0.04	GO2063
203004488	16 18 44.316	−27 35 30.40	⋯	1.35	5	0.08	GO2063
204250417	16 15 13.612	−23 04 26.12	M6.5[b]	1.28	7	0.10	GO2045
K2 C15							
203590915	15 50 59.935	−25 37 11.66	⋯	0.76	6	0.03	GO15043
249146655	15 42 08.305	−26 21 13.84	M5.7[d]	0.38	7	0.02	GO15043
249202312	15 41 55.626	−25 38 46.53	⋯	1.42	7	0.03	GO15043

Notes. R.A., decl., and proposal ID from *K2* MAST Archive. The period, the number of segments with the same period, and its uncertainty is listed, followed by the proposal ID for each object.
[a] Bouy & Martín (2009).
[b] Slesnick et al. (2008).
[c] Lodieu et al. (2011).
[d] Dawson et al. (2014).

clarity, we include Figure 2 showing the steps of our period search as described above.

In sample A, we measure a total of 25 periods. 22 (88%) of them were consistent in five or more segments, while the remaining 3 (12%) were found in three or four segments of the light curve. In sample B, 79 periods were detected. Sixty-five of them (82.3%) were consistent in five, six, or seven segments, while the other 14 (17.7%) were found in two, three, or four segments. Our 25 accepted periods for sample A are shown in Table 1, with uncertainties calculated as the standard deviation between segments for which the period was confirmed. Sample B adds another 79 periods, which are shown in Table 2. Our period search, then, resulted in period measurements for 104 out of the 204 objects altogether. We show phased light curves for all 104 periodic objects in the Appendix.

3.3. Comparison with Literature

In Figure 3 we show our periods in comparison with previously published measurements in the literature, for A and B samples separately.

For sample A, we independently recover 13 periods from Scholz et al. (2015), including their noted outlier EPIC 203348744, which they measured as $P \sim 5$ days; for the other

3 objects, a period could not be adequately determined from the K2SFF light curve using ACF and visual inspection, and thus they are excluded from our sample. Our periods are in agreement, within the uncertainties, with Scholz et al. (2015) with the exception of EPIC 204439854, where we find a period half their measured value. A period was previously published for EPIC 203083616 (Cody & Hillenbrand 2018; Hedges et al. 2018); our value is half that of their measurement. These 14 objects are shown as black circles in the left panel of Figure 3. In this figure, we show the 1:1 relation (solid line), the lines corresponding to 10% deviation (dashed) and for factor-of-two discrepancy (dotted–dashed).

Twenty-two of the objects from sample A and all 79 from sample B have measured periods in Rebull et al. (2018), shown in Figure 3 as well as cyan circles. Most (98/101) Rebull periods are in agreement (within 10%) with our measured periods, between the two samples. For the remaining three objects, the periods are roughly multiples of ours: for EPIC 203083616 and EPIC 204439854, our measured period is half that measured by Rebull, and for EPIC 204418005, it is one-quarter the literature value. In contrast to the ACF-based period search on segmented light curves used here, Rebull et al. (2018) apply Lomb–Scargle periodograms on the entire light
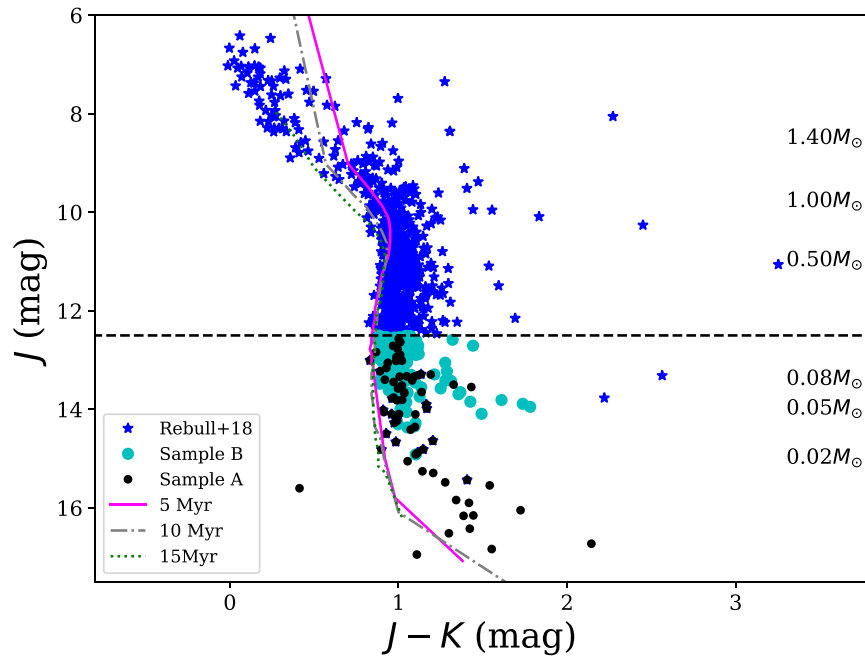
Figure 1. $(J, J - K)$ color–magnitude diagram, displaying our sample selection. The 5, 10, and 15 Myr isochrones are taken from Baraffe et al. (2015), shifted from absolute magnitude to apparent magnitude using a distance to Upper Sco of 145 pc (Cook et al. 2017). Objects from Rebull et al. (2018) are shown as blue star symbols, while our A and B samples are displayed in black and cyan, respectively.

curve. In summary, the comparison with the literature confirms the validity of our period sample.

3.4. Injected Periods

We do not find any periods $\lesssim 0.20$ day or $\gtrsim 5$ days in our ACF period search of K2SFF light curves. To test the validity of these limits, we create data sets with 100 different sinusoidal periods (0.1–10 days, in steps of 0.1 day), each with two different amplitudes (0.015 and 0.03, measured from zero to peak), typical for the periodicities that we found. We inject these periods into nonperiodic light curves from three different objects, to retain the noise and sampling of K2. These three objects cover the range of J-band magnitudes seen in our sample: EPIC 202978875 ($J = 12.939$), EPIC 202633073 ($J = 14.097$), and EPIC 204341806 ($J = 16.947$); this provides a sample of 600 injected periods. We then perform a period search using our ACF process, dividing each injected light curve into seven segments. A period is recovered if it is found in multiple segments with <0.1 day tolerance. Due to the large number of injected periods, we do not perform the visual examination as we did during the period search. Figure 4 shows the relative discrepancy between injected and recovered period versus the injected period. Objects for which a period was not recovered are plotted at a relative discrepancy of 0.5; for the smaller amplitude, this corresponds to 68 points, and 40 points for the larger amplitude. In total, 108/600 (18%) of the injected periods are not recovered. We successfully recover 173 periods for the smaller amplitude, and 198 for the larger amplitude. Overall, 371/600 or 61.8% of injected periods are recovered. For the remaining 121 test light curves we find a period, but not within 10% of the injected period. In summary, the injection test demonstrates that the method is sensitive to a wide range of periods, although we will be incomplete for amplitudes of <0.015 and for periods >4 days.

3.5. Period Distributions

Figure 5 shows the histograms of the period distributions for sample A (green) and sample B (cyan), with and without the single long-period outlier at 4.29 and 4.26 days, respectively. The dashed red and magenta lines denote the average of samples A and B respectively, while the black dashed line represents the average for the sample from Scholz et al. (2015). The periods for sample A range from 0.21 to 1.77 days (excluding the aforementioned outlier), with a mean and median of 1.10 and 0.97 days (0.97 days and 0.97 days, respectively, without the outlier). For sample B, the range (again, excluding its outlier) for the period distribution is from 0.29 to 2.93 days; the mean and median are 1.34 and 1.33 days, respectively (1.30 and 1.33 days without the outlier). Our period samples broadly confirm the previously found distribution, but expands the sample size considerably. The similar means and medians also suggests that there are no systematic differences in the period distributions for samples A and B. For the full sample of 104 periods, the median is 1.28 days. Selecting only the probable brown dwarfs adopting $J = 13.3$ as a threshold, the median drops to 0.84 days. Thus, with very few exceptions, brown dwarfs at the age of Upper Sco are fast rotators with typical periods around 1 day and with very few exceptions below 3 days. All this is in line with findings by other authors (Rodríguez-Ledesma et al. 2009).

3.6. Brown Dwarfs versus Stars

Figure 6 shows the Upper Sco periods from Rebull et al. (2018) and our measured brown dwarf periods, from both A and B samples, versus 2MASS J magnitude. Again we excluded the younger ρ Oph region (see Section 2). As expected from our sample selection, the targets are all on the faint end of this diagram, and are expected to have masses below or around the substellar boundary. In contrast, the Rebull et al. (2018) sample includes the entire stellar mass range.
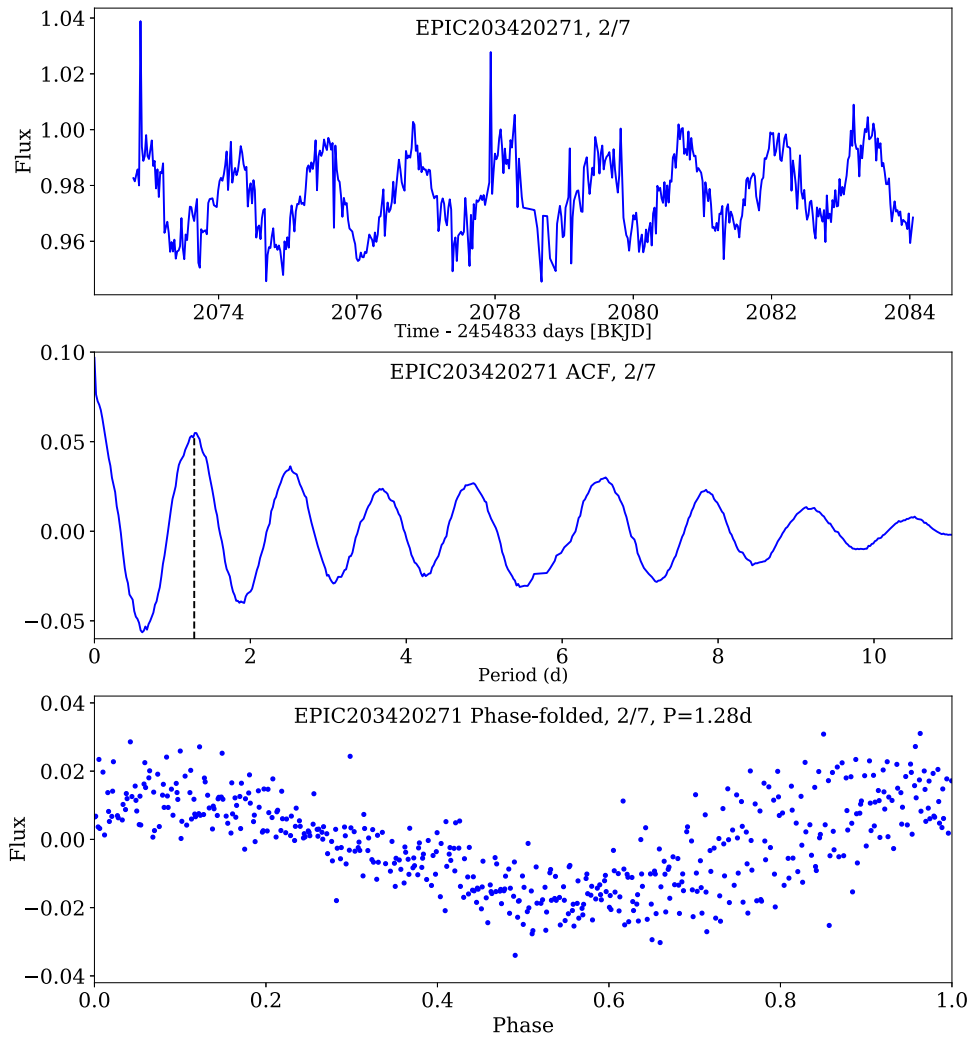
Figure 2. Our period search process, illustrated here for EPIC 203420271. After visual inspection of the entire light curve, we note that there is a periodic signal. We then divide the light curve into seven segments, all of which show periodicity. The top panel shows the second of these seven segments. The calculated autocorrelation function is shown in the middle panel, with a clear peak at zero, and a strong peak at 1.28 days. The bottom panel shows the phase-folded light curve, after subtraction of the average flux, using the identified period of 1.28 days from the ACF.

Assuming that the objects are roughly coeval and not significantly affected by extinction, the J-band magnitude serves as a proxy for mass. Approximate mass limits are overplotted in Figure 6 from the Baraffe et al. (2015) tracks and adopting a distance of 145 pc.

Similar to previously studied star-forming regions, the periods in Upper Sco show a strong mass dependence. The average period and the range of periods drop significantly with mass, as found previously in the ONC (Rodríguez-Ledesma et al. 2009) and NGC 2264 (Lamm et al. 2005). The mean period in our samples is 1.10 days, whereas the average in the periods for stars in Upper Sco is more than three times as long (3.38 days). While brown dwarf periods predominantly cluster below 3 days, more massive stars show a much wider range of periods up to several weeks.

Figure 6 also reveals that we do not find periods for the low mass brown dwarfs in the samples: whereas the magnitude distribution of the samples extends to $J \sim 17$ and $0.02\,M_{\odot}$, the period sample has a lower limit at $J < 15$. Thus, the period sample is dominated by high-mass brown dwarfs and very low mass stars. This is further illustrated by Figure 7 which shows the recovery rate for periods as a function of magnitude. For

sample A, we only recover periods for objects up to $J = 15$, mostly for the brightest objects between $J = 12$–13. While sample A includes objects in the $J > 15$ bins (up to $J \sim 17$), we do not find any periods for these fainter objects. Since sample B only includes objects with $J < 15$, we recover periods in all magnitude bins. Future observations with greater depth should aim to measure rotation periods for the faint objects in this region.

4. Disks versus Rotation

4.1. Identifying Disks

To test for the presence of disks, we compile photometry from the *Wide-field Infrared Survey Explorer* (Cutri et al. 2013) in the channels $W1$ to $W4$, corresponding to wavelengths of 3.4, 4.6, 12, and 22 μm. While longer wavelengths such as $W3$ and $W4$ would be ideal to identify disks, only 19 of our 69 objects from sample A have an S/N > 5.0 in $W3$, and only 4 of these 69 objects have an S/N > 5.0 in $W4$. The numbers are similar for sample B. Therefore, we use the $W1 - W2$ color excess as primary evidence of a disk. For the remainder of the paper, we

Table 2
Sample B Period Catalog

EPIC ID	R.A.	Decl.	P_{ACF}	N	ΔP
204077926	15 55 30.601	−23 45 21.27	1.00	5	0.02
204862399	15 55 52.727	−20 31 33.62	0.29	7	0.0
204107757	15 56 01.043	−23 38 08.12	1.53	4	0.02
204269918	15 56 23.402	−22 59 49.12	0.82	5	0.01
204229193	15 56 40.196	−23 09 29.13	1.79	5	0.05
204442667	15 57 28.490	−22 19 05.11	1.29	5	0.03
204849054	15 57 56.034	−20 35 10.48	0.97	6	0.02
204238921	15 58 39.896	−23 07 10.67	1.98	4	0.03
204594600	15 58 48.133	−21 41 33.88	0.60	6	0.02
204367110	15 59 12.444	−22 36 50.22	0.96	4	0.02
204247509	15 59 25.919	−23 05 08.20	0.60	7	0.01
203574463	15 59 49.546	−25 40 34.26	0.98	7	0.01
204769599	16 00 26.698	−20 56 31.61	1.61	5	0.06
204121833	16 00 30.236	−23 34 45.71	0.46	6	0.02
204435603	16 01 49.508	−22 20 45.18	1.55	6	0.05
204054129	16 01 49.559	−23 51 08.20	0.52	7	0.03
203708909	16 02 06.835	−25 12 38.51	1.14	7	0.03
204258708	16 02 09.557	−23 02 27.73	0.48	7	0.02
204178534	16 02 12.804	−23 21 20.20	1.37	6	0.04
204417649	16 02 25.984	−22 24 57.50	1.42	6	0.04
203514056	16 04 22.562	−25 53 03.86	2.18	6	0.05
205164304	16 06 31.108	−19 04 57.65	2.17	3	0.04
204878461	16 07 35.558	−20 27 13.46	1.81	7	0.03
204397408	16 08 10.817	−22 29 42.85	1.62	5	0.06
204472612	16 08 34.552	−22 11 55.92	1.79	3	0.04
205142340	16 08 35.779	−19 11 37.27	1.27	7	0.02
205358744	16 08 36.593	−18 02 49.75	1.28	5	0.02
205092303	16 09 20.545	−19 26 31.87	1.74	5	0.09
203581504	16 09 26.957	−25 39 08.16	0.60	7	0.01
204756726	16 09 30.190	−20 59 53.62	1.51	4	0.07
203362293	16 09 30.236	−26 23 41.64	1.02	7	0.03
204769996	16 09 36.079	−20 56 25.59	1.72	6	0.02
204783273	16 09 37.069	−20 52 52.98	1.08	7	0.03
203065387	16 09 51.077	−27 22 41.88	0.54	7	0.02
204472125	16 09 56.959	−22 12 02.70	0.79	6	0.02
204538466	16 09 59.908	−21 55 42.50	0.84	7	0.04
204551703	16 10 01.294	−21 52 24.36	1.67	5	0.03
203692610	16 10 31.627	−25 16 01.71	1.83	6	0.04
204870669	16 10 35.249	−20 29 16.86	1.37	7	0.05
205241182	16 10 46.362	−18 40 59.87	2.07	4	0.04
204468732	16 10 49.962	−22 12 51.59	0.76	7	0.04
204561327	16 11 09.200	−21 49 56.25	0.95	7	0.05
205355375	16 11 18.211	−18 03 58.55	1.12	7	0.02
204365837	16 11 31.805	−22 37 08.23	1.66	7	0.08
204292655	16 11 45.301	−22 54 32.92	1.60	6	0.07
205086621	16 11 45.344	−19 28 13.23	1.70	5	0.01
204803505	16 12 11.858	−20 47 26.72	4.26	7	0.10
205102553	16 12 18.454	−19 23 32.46	1.85	6	0.07
204651122	16 12 22.900	−21 27 15.87	1.52	2	0.01
204928499	16 12 27.040	−20 13 25.04	0.89	7	0.04
204940701	16 12 27.378	−20 09 59.69	1.87	2	0.05
204245943	16 12 45.065	−23 05 30.33	0.73	6	0.02
205167772	16 12 47.268	−19 03 53.16	1.16	7	0.04
204888409	16 12 48.974	−20 24 30.29	1.36	6	0.04
205082248	16 13 03.068	−19 29 31.91	1.71	6	0.06
204259310	16 13 09.829	−23 02 18.44	1.33	4	0.02
205097920	16 13 28.092	−19 24 52.43	1.46	7	0.04
204299578	16 15 15.192	−22 52 53.75	0.77	7	0.05
204584778	16 15 25.168	−21 44 01.32	1.68	5	0.07
205198363	16 15 33.415	−18 54 25.00	1.89	6	0.05
204621457	16 15 41.108	−21 34 46.46	0.57	7	0.03
204467371	16 15 49.144	−22 13 11.77	1.77	7	0.04
204199333	16 16 11.842	−23 16 26.81	0.81	7	0.03
203710387	16 16 30.684	−25 12 20.17	2.79	3	0.02

Table 2
(Continued)

EPIC ID	R.A.	Decl.	P_{ACF}	N	ΔP
204099505	16 17 21.185	−23 40 08.63	1.99	6	0.03
205596184	16 18 03.053	−16 30 15.22	2.01	4	0.04
204435866	16 19 23.934	−22 20 41.25	1.38	7	0.09
204260042	16 19 50.927	−23 02 08.16	1.31	7	0.05
204287798	16 20 26.092	−22 55 42.88	0.97	7	0.01
204346718	16 21 16.816	−22 41 36.69	0.64	7	0.03
203001378	16 21 54.806	−27 36 10.28	2.93	3	0.01
204449274	16 22 21.605	−22 17 30.70	1.53	4	0.03
204611501	16 23 01.115	−21 37 17.00	2.38	7	0.08
204683343	16 23 04.751	−21 18 59.34	0.46	7	0.02
202906224	16 23 17.617	−27 56 10.96	0.71	7	0.03
202709152	16 23 31.168	−28 39 17.65	0.73	7	0.03
204195050	16 23 51.558	−23 17 27.03	0.48	7	0.01
205431449	16 34 27.743	−17 37 31.71	0.46	6	0.03
204220275	16 11 40.405	−23 11 34.77	1.32	6	0.06

combine sample A and sample B into a single sample to simplify the analysis.

In Figure 8 we show the $W1 - W2$ color versus J-band magnitude for the entire sample. There is a clear separation in $W1 - W2$ color between objects with and without excess. According to Pecaut & Mamajek (2013), the $W1 - W2$ color is 0.21–0.34 for spectral types M5–M7 (their Table 6), which should be the location of the photosphere in Figure 8. The majority of our sample falls nicely into this range. We define a cutoff 2σ to the right of the typical photospheric $W1 - W2$ and use it as a threshold to identify objects with IR excesses and thus disks. This threshold is shown in Figure 8 as a dashed line and corresponds to $W1 - W2 \gtrsim 0.32$.

We note that at the low mass end of the diagram ($J > 15$) the photospheric $W1 - W2$ color is likely to exceed our adopted threshold of 0.32 and increase to 0.2–0.4. As we do not find periods in this magnitude range, however, this ambiguity is irrelevant for the present discussion. Based on our simple criterion, we identify that 60 of our 204 objects have a disk. Of the objects with disks, 21 have a measured period, while 39 do not.

4.2. Disks versus Rotation

Figure 9 plots our measured periods against $W1 - W2$ color, with the horizontal black dashed line indicating the dividing line between objects with disks and those without at $W1 - W2 = 0.32$. For the entire sample, the median is 1.61 days for objects with disks and 1.03 days for those without. These median periods are overplotted in Figure 9. Thus, the disk-bearing objects rotate on average slower than their diskless counterparts; their median period is about 50% longer.

To compare the period distributions on the two sides of the threshold shown in Figure 9, we perform a Kolmogorov–Smirnov (or KS) test and find that they are unlikely to be drawn from the same distribution, with a false alarm probability of 0.003%. Furthermore, if we randomly pick 10,000 subsamples of periods that are identical in size to the number of periods with disks (25), the probability of getting a median of 1.5 days or longer is less than 1%.
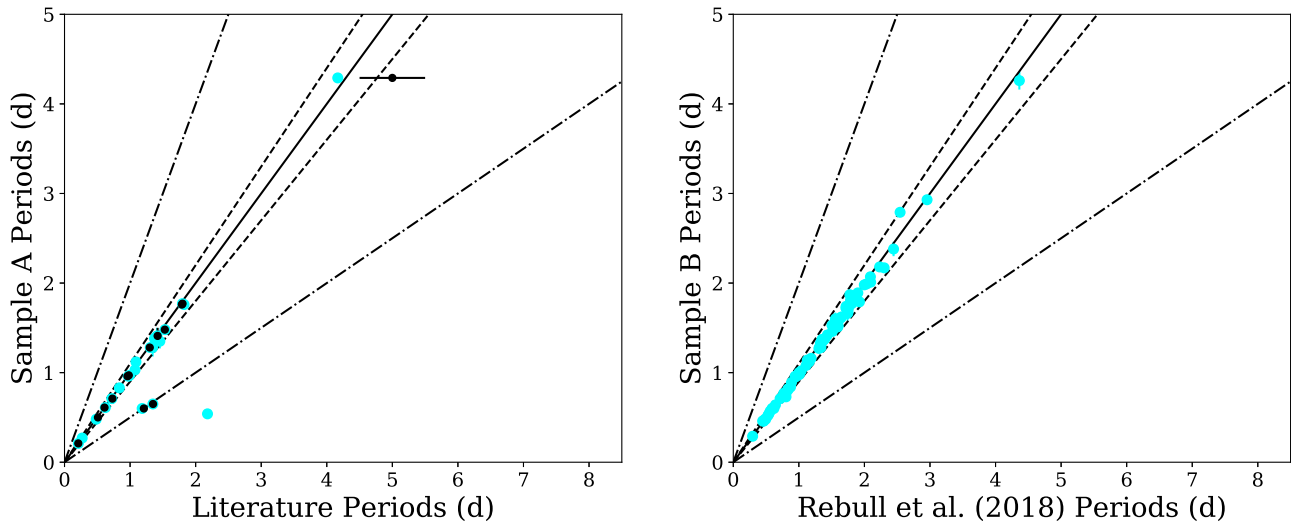
Figure 3. Comparison of the periods for samples A (left panel) and B (right panel) with those in the literature. In the left panel, the black circles indicate comparisons with Scholz et al. (2015), Cody & Hillenbrand (2018), and Hedges et al. (2018), while, in both panels, cyan circles indicate comparisons with Rebull et al. (2018). It is clear that there is a strong correlation between our measured periods and those in the literature. The black dashed line in both panels indicates $y = x$, i.e., a perfect agreement, while the black dashed lines show $y = 1.1x$ and $y = 0.9x$, a 10% discrepancy, and the black dotted–dashed lines show $y = 2x$ and $y = 0.5x$, i.e., period disagreeing by a factor of two. Uncertainties included for Scholz et al. (2015), but not published in Cody & Hillenbrand (2018), Hedges et al. (2018), or Rebull et al. (2018).
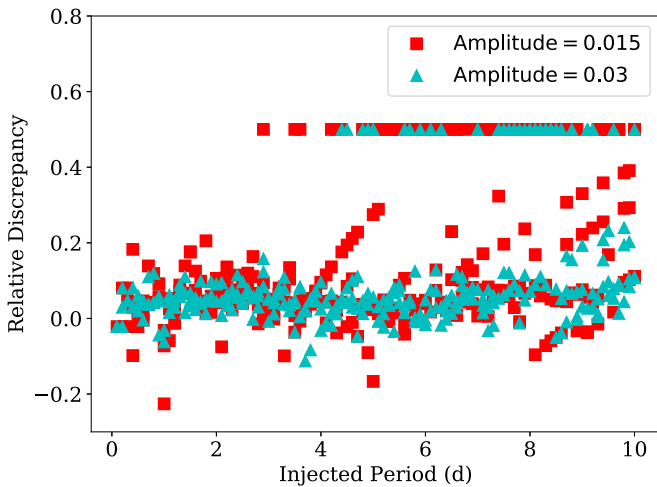
Figure 4. Plot of relative discrepancy vs. injected period, for our 100 injected periods and two different amplitudes in three different light curves without a measured period. Here, we define relative discrepancy as (injected period—recovered period)/injected period. It is clear that the majority of our ACF-measured values are within 10% of the injected value. See the text for more details.

We repeat this analysis after isolating the brown dwarfs, using only objects with $J > 13.3$ (the likely threshold between stars and brown dwarfs for an assumed age of 8 Myr). The period sample after this step versus IR color is shown in Figure 10. This leaves 32 periodic objects, 10 of which have a disk. After the $J > 13.3$ cut, the results do not change significantly. We find a median period of 1.52 days for objects with disks, and a median period of 0.75 days for objects without disks. Again, the median periods for the samples with disks are found to be longer than for the ones without, by a factor of about 2. The KS test results in a probability of 1.6% that the two distributions are drawn from the same population. The chances of picking a subsample with a median period equal to or larger than the one measured for brown dwarfs with

disks is increased, due to the small number of objects, but still in the range of 10%.

In summary, our analysis supports the idea that the presence of disks in brown dwarfs and very low mass stars is linked to slow rotation, in line with what is expected for rotational braking due to a disk. While objects with disks are predominantly slow rotators, the ones without disks are spread over a wide range of periods, including a subset of slow rotators. In the standard disk-braking paradigm this is usually understood as an evolutionary effect—slow rotators without disks are objects that have recently ceased disk braking and lost their disks, hence they did not have enough time yet to spin-up, as discussed, for example, in Rebull et al. (2006) and Vasconcelos & Bouvier (2015).

5. Dippers in the Upper Sco Period Sample

Given the evidence for a link between slow rotation and the presence of disks in Section 4, we searched in the light curves for direct signs of disk locking among our targets. A fraction of young stars shows regular "dips" in the light curve (McGinnis et al. 2015), similar to the prototype for this behavior, AA Tau. For many of these "dippers," the preferred explanation is a warp in the inner disk that periodically occults parts of the central object and is caused by magnetospheric accretion. In many cases, the period of the dips is similar to the rotation period of the star, i.e., the star is "locked" to the inner disk. Stauffer et al. (2015) identify a subcategory of dippers with short-duration and shallow dips among young stars. Dippers have recently been found in the Upper Sco region as well (Ansdell et al. 2016; Cody & Hillenbrand 2018; Hedges et al. 2018).

In Figure 11 we show the *K2* light curves for two brown dwarfs in our A sample, EPIC 204083616 and EPIC 204344180. These two show clear signs of multiple dips in the light curve. Both have been identified as dippers previously in the literature, the former by Hedges et al. (2018) and Cody & Hillenbrand (2018), the latter by Scholz et al. (2015) and Cody & Hillenbrand (2018). For both objects, we also find sinusoidal
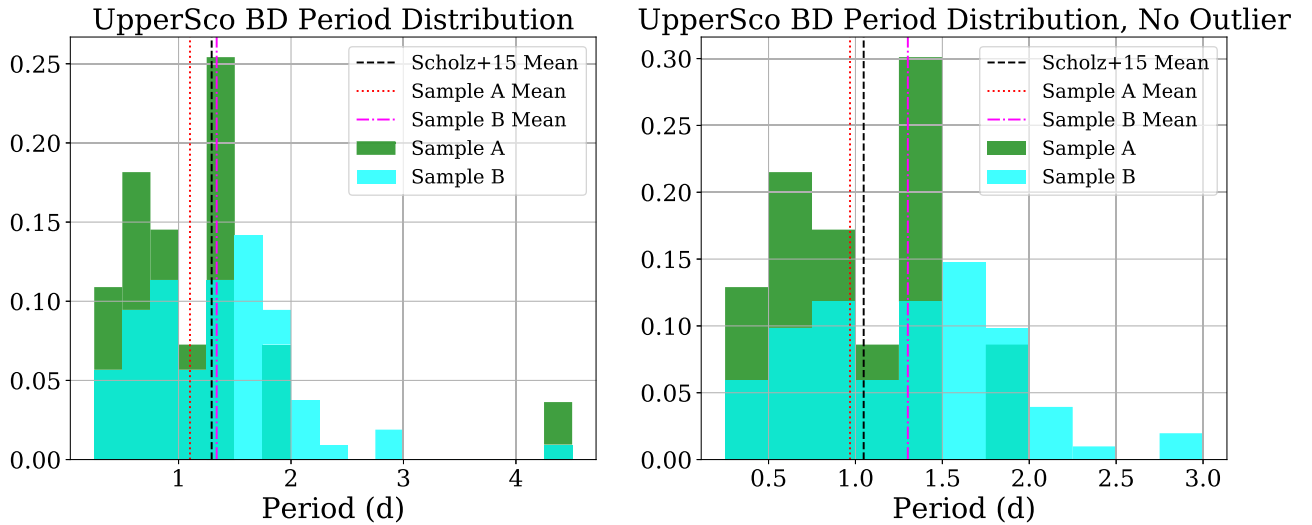
Figure 5. Period distribution of samples A (green) and B (cyan). The left panel shows all periods from our catalog, and the right panel shows the distribution after removal of the single long-period outlier. The red dashed lines are the average of sample A (with and without the outlier), the magenta lines are the average of sample B periods (also with and without the outlier). For comparison, the black dashed lines are the average of the 16 periods (or 15, after removal of the outlier, in the right panel) from Scholz et al. (2015).
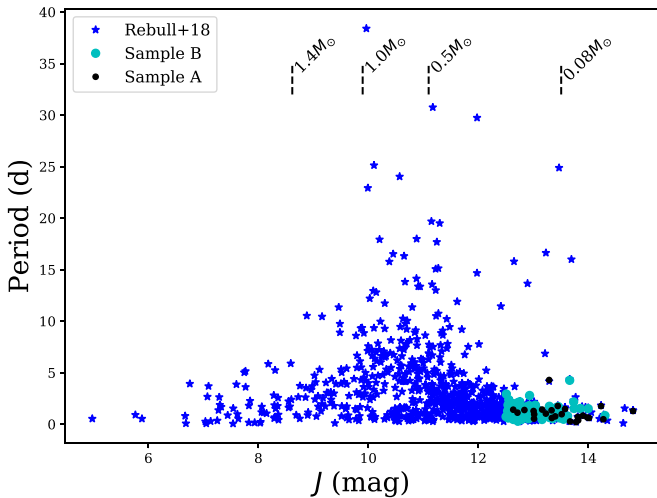
Figure 6. Comparison of Upper Scorpius stellar periods (Rebull et al. 2018; blue star symbols) and brown dwarf periods (our sample A, black circles, and sample B, cyan circles) plotted against 2MASS J magnitude. Mass limits determined by converting M_J from the 10 Myr isochrones of Baraffe et al. (2015) to apparent magnitude J, using a distance of 145 pc.

variability with consistent periods in six out of seven segments in the light curves, which we interpret as rotation periods. These two also host disks. With J-band magnitudes around or below 14 and little extinction ($J - K \sim 1$), both are safely in the substellar domain, irrespective of the assumed age for Upper Sco. Thus, the dipper phenomenon is observed among brown dwarfs as well, confirming that magnetospheric accretion is a process universally found across the stellar and substellar mass spectrum (Scholz et al. 2005).

For both cases, the duration of the dips is in the range of 0.5–1 day. As reported in Scholz et al. (2015), EPIC 204344180 shows deep eclipses with a variable depth of up to 40% in the first 20 days of the $K2$ light curve, and only occasional and less pronounced dips in the remainder of the data set. EPIC 204083616's light curve features persistent dips with depths of up to 20% throughout, although the depth

diminishes in the second half of the observing run. A more detailed analysis of the light-curve morphology and a more complete assessment of the dipper fraction among brown dwarfs is postponed to a future paper.

In the context of this paper, it is important to compare the separation between the dips with the rotation period, as in a disk-locking scenario the warp in the inner disk (causing the dips) should be corotating with the central object. In Figure 12 we show the same light-curve segments from Figure 11 in phase to a period of 1.35 days for EPIC 204083616 and 1.8 days for EPIC 204344180, illustrating the periodicity in the dips. This figure also shows the additional sinusoidal variation, which is much more clearly visible in the second half of the light curves when the dips in these two cases have subsided. For EPIC 204344180 the rotation period is 1.76 days, close to the dipper period. For EPIC 204083616, we measure a rotation period of 0.65 days, but two other papers find a rotation period about double this value (Cody & Hillenbrand 2018; Hedges et al. 2018), which would be very similar to the dipper period. Thus, pending confirmation of the longer period for EPIC 204083616, the features in the disk causing the dips are likely to be corotating with the central objects. Assuming Keplerian rotation, the periods of the dips indicate that the warp has to be located around 0.01 au distance from the central object, which is approximately where we expect the inner edge of the disk for this type of object (Scholz et al. 2007). Thus, for these two objects there is direct evidence for locking between the rotating brown dwarf and the inner disk.

6. Rotation versus Age

With the rotation periods for brown dwarfs in Taurus and Upper Scorpius in hand, now we have two sizable samples of periods from $K2$ to investigate the early rotational evolution of substellar objects. With the uniform 30 minute cadence of *Kepler*, these two samples cover the entire plausible period range for such objects. In addition, the targets are well characterized, with spectroscopic and kinematic confirmation of youth for many of them. Ground-based samples from the literature provide additional constraints. The following section
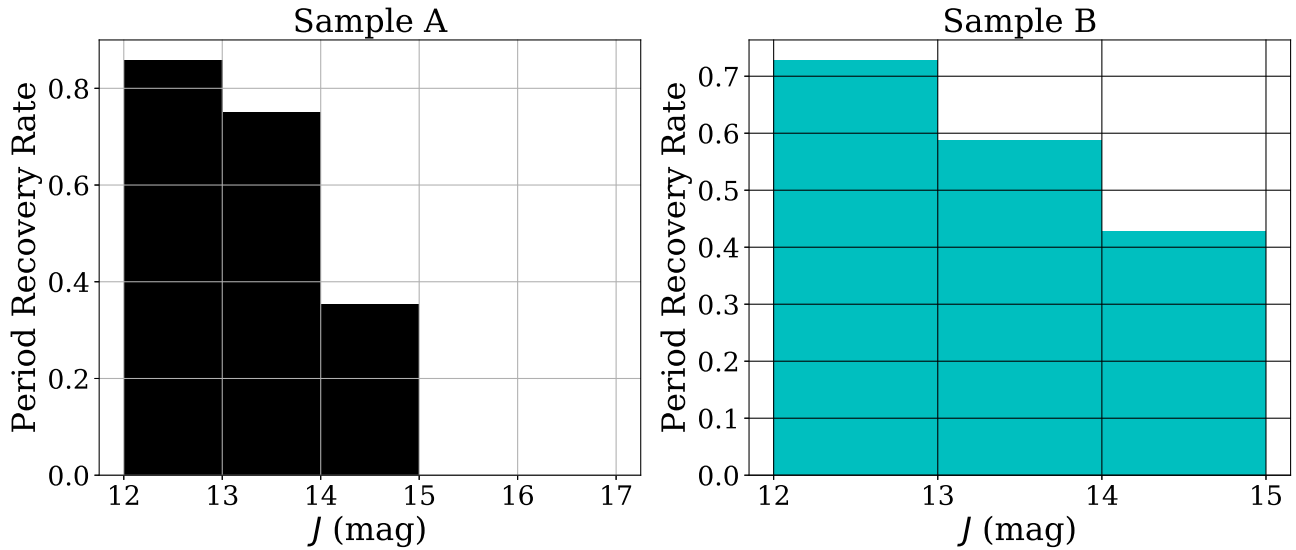
Figure 7. Period recovery rates of sample A (left panel, black) and sample B (right panel, cyan) as a function of their *J*-band magnitude. We divide the samples into bins of width $J = 1$; sample A contains objects with $J \sim 12\text{–}17$, while sample B contains objects with $J \sim 12\text{–}15$. As can be seen, we recover significantly more periods for brighter objects, with a steady decrease as the objects become fainter. Note that, although sample A contains objects in the $J = 15\text{–}17$ bins, we do not recover any periods in that magnitude region.
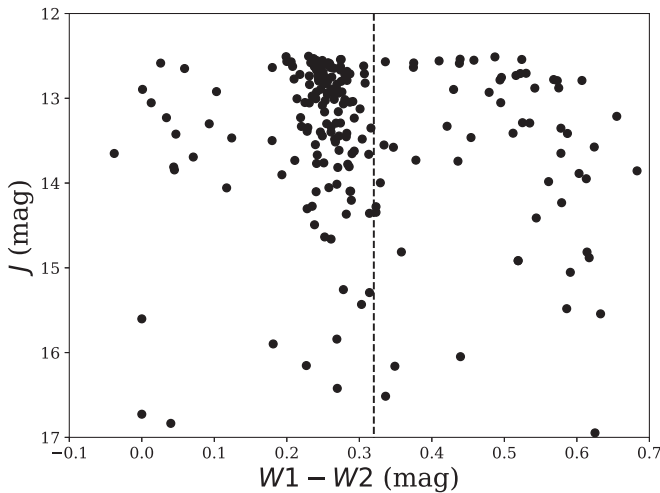
Figure 8. $(W1 - W2, J)$ color–magnitude diagram. Our disk cutoff is determined by taking 0.21–0.34 as the photospheric location for objects with SpT M5–M7 (Pecaut & Mamajek 2013), and defining a cutoff 2σ to the right; this $W1 - W2$ disk cutoff is shown as the vertical black dashed line. Objects to the left of this line are then defined to be diskless, while objects to the right are disk-bearing.
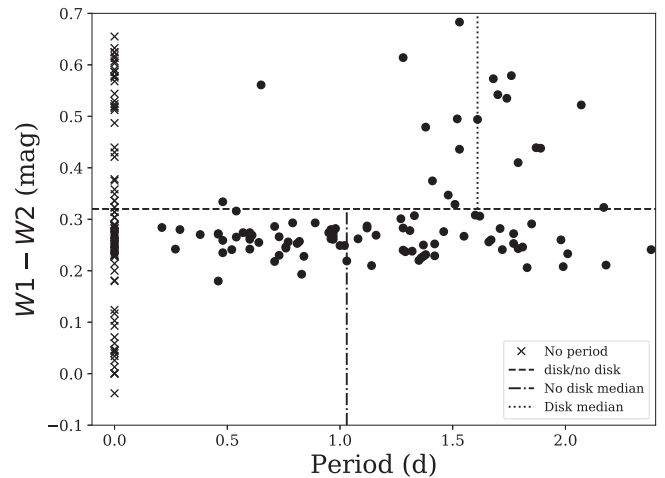
Figure 9. $(W1 - W2)$ color vs. period, indicating the presence of a disk. EPIC 203348744, the sample A period outlier with 4.29 days, and EPIC 204803505, the sample B period outlier with 4.26 days, are not visible on this plot, but fall above and below this limit, respectively. The medians for diskless (dotted–dashed) and disked objects (dotted) are shown, above and below the $W1 - W2$ disk cutoff. Objects without measured period are plotted at $P = 0.0$ days as black x symbols.

is an update and improvement on the discussion in Scholz et al. (2015).

In Figure 13 we show the available period samples for young brown dwarfs as a function of age. The diagram includes periods from Taurus (Scholz et al. 2018) and Upper Sco (this work), plus the ground-based samples in the ONC (Rodríguez-Ledesma et al. 2009) and the Orion belt region (Scholz & Eislöffel 2004a, 2005; Cody & Hillenbrand 2010). The latter comprises periods for members of the clusters around the σ Ori cluster and the ϵ Ori cluster, which we group together here. Overplotted are the median and 10th/90th percentiles for all four samples. Typical ages are used, based on the literature review in Scholz et al. (2015), but in all cases age uncertainties and age spreads are possible sources of confusion.

In comparison to Figure 4 in Scholz et al. (2015), this plot features the additional periods from *K2* and improves the homogeneity of the period samples. In particular, given that period depends on mass, it is essential to make sure that the samples have comparable mass ranges and do not include a significant fraction of stars. Therefore, we refined all samples by defining cutoffs in absolute *J*-band magnitude to separate stars from brown dwarfs. In all samples, the lower mass limits are comparable and at $0.02\,M_\odot$; besides, the samples are dominated by high-mass brown dwarfs. It is the upper mass limit that needs a critical assessment before analyzing the evolution.

For the ONC sample from Rodríguez-Ledesma et al. (2009) this step necessitates an extinction correction. We use the near-infrared magnitudes published in Rodríguez-Ledesma et al. (2010)
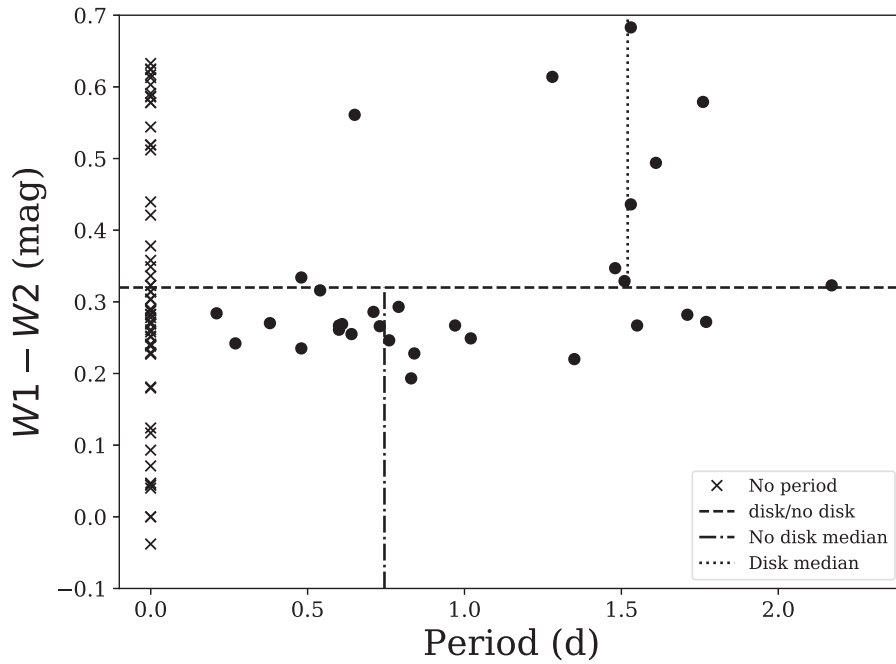
Figure 10. Same as Figure 9, but after a cut has been made to both samples at $J > 13.3$, to isolate brown dwarfs. Again, the medians for diskless (dotted–dashed) and disked objects (dotted) are shown, above and below the $W1 - W2$ disk cutoff, and objects without measured periods are plotted at $P = 0.0$ day as black x symbols.
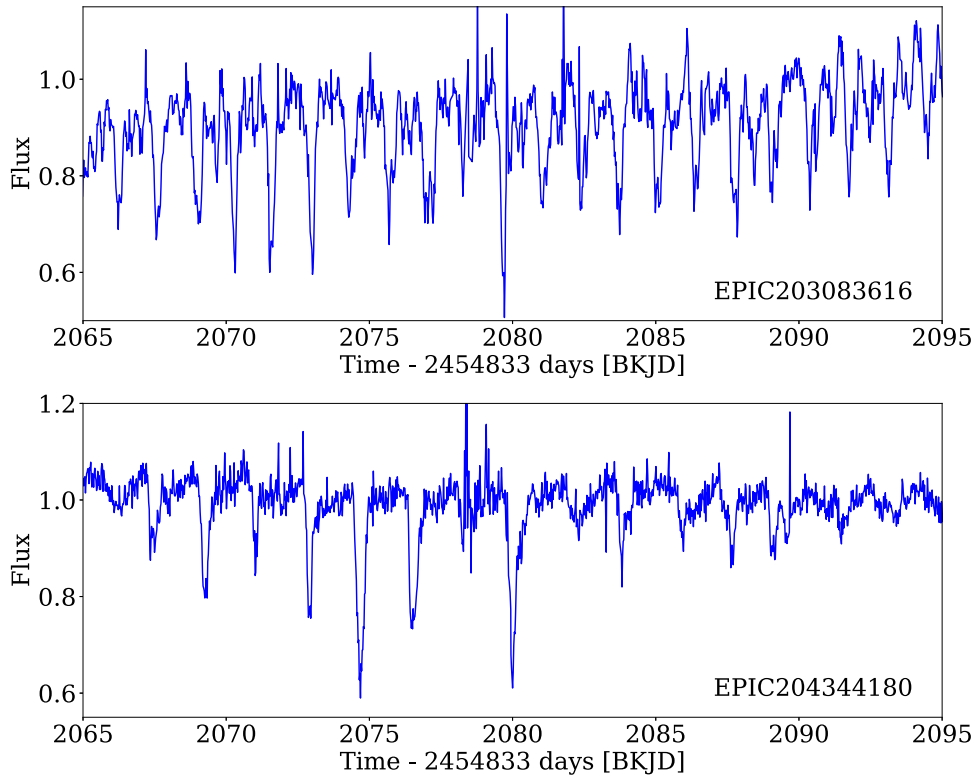

Figure 11. Partial $K2$ light curves for two brown dwarfs in our sample that show the signature of a "dipper," i.e., transient and/or variable eclipses, in addition to showing a more sinusoidal variation throughout the observing campaign.

to calculate A_V from the $J - K$ color, following the recipe described in Scholz et al. (2018). We then deredden the J-band magnitude, calculate the absolute magnitude using $m - M = 8$ (Kounkel et al. 2018), and impose a cutoff at $M_J = 6$ to select brown dwarfs. This threshold is informed by the 1 Myr isochrone from Baraffe et al. (2015). Some brown dwarfs will be affected by

near-infrared excess due to disks; for those we will overestimate A_V and thus might remove them from our sample. We are, however, not aiming for a complete sample here; it is more important to make sure the list of periods is not contaminated by embedded, reddened stars. The resulting sample of ONC periods comprises 98 likely brown dwarfs.
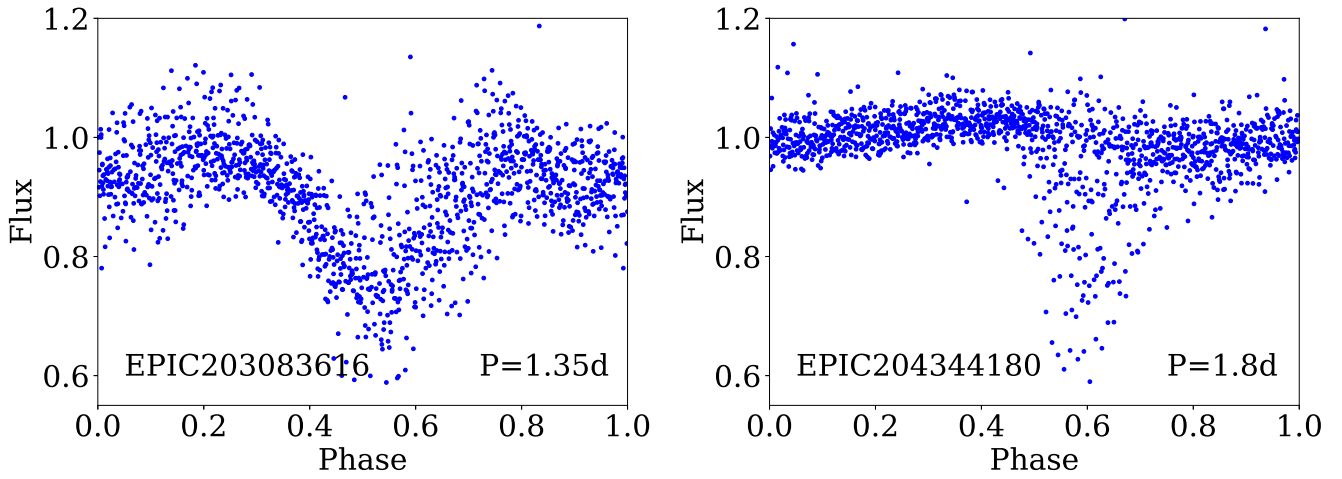
Figure 12. Phased light curves for the two segments shown in Figure 11, demonstrating that the dips are occuring periodically, although they are varying in depth and duration.
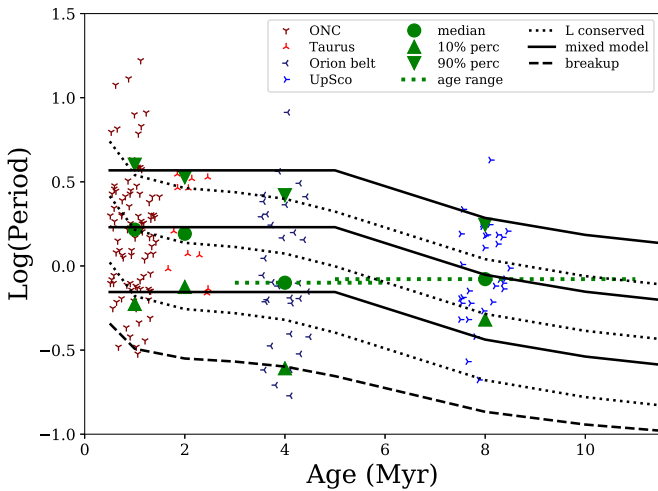
Figure 13. Rotation period vs. age for brown dwarfs in star-forming regions. Median and 10/90% are also overplotted in large green symbols. The model tracks (black lines) are calculated using evolutionary tracks by Baraffe et al. (2015). In the case of the solid lines, they include 5 Myr of disk locking, for the dotted lines no disk locking is assumed. The breakup period is also overplotted as dashed line. For clarity, the data points in the individual regions are scattered randomly around a mean age.

The Orion belt regions are free of excessive extinction, and thus contamination by reddened stars is less of a concern. We obtain J-band magnitudes from 2MASS for the sample from Cody & Hillenbrand (2010) in σ Ori, remove nonmembers according to the classification in the original paper, correct for the distance (again with $m - M = 8$), and adopt a cutoff of $M_J > 6.5$ to pick brown dwarfs, resulting in 13 objects. For the literature samples from Scholz & Eislöffel (2004a) and Scholz & Eislöffel (2005) we use the masses provided in the original papers to pick brown dwarfs. These masses are estimated based on a comparison of near-infrared photometry with Baraffe et al. evolutionary tracks, consistent with our method here. Altogether, the Orion belt sample comprises 32 brown dwarfs.

For the Taurus sample, we estimated absolute J-band magnitudes in Scholz et al. (2018), including an extinction correction. We adopt a threshold of $M_J = 6$ boundary between

stars and brown dwarfs, consistent with the cutoff in the ONC, which leaves a total of 12 periods. As described in Section 2, the Upper Sco sample may include very low mass stars. To minimize contamination, we reduce the sample using a J-band cutoff of 13.3, corresponding to $0.08\,M_\odot$ for an age of 8 Myr, according to Baraffe et al. (2015). This is a compromise between the minimum and maximum values for the age of Upper Sco determined in the literature, resulting in a sample of 32 brown dwarfs with periods.

When comparing period samples from multiple observing runs with varying cadence and duration, it is important to keep in mind possible observational biases. The two samples from *K2* have been derived from homogeneous data and with the same period search method, therefore we can expect a similar period sensitivity. As demonstrated in Section 3, our method robustly finds periods between 0.1 and 10 days, limits that are beyond the actual period range. Therefore, these two samples are the most important constraints on the rotational evolution. It is also reassuring that the distribution of the ONC periods are broadly comparable with the Taurus periods from *K2*, both in terms of the median and in the upper/lower limits.

In contrast, the sample for the Orion belt does show anomalies compared to the other three. For one, it exhibits clear substructure, including a large gap around a period of 1 day. When monitoring from the ground, periods of a few hours and those of several days are typically easier to find than those around 1 day, as shown, for example, in Scholz & Eislöffel (2004a). The upper limit is affected by the duration of the ground-based observing runs, which do not all cover the entirety of the period range. As a result, typical periods (median, upper/lower limit) are likely to be significantly underestimated. From Figure 13, it is obvious that the lower limit and median in the Orion belt sample are markedly lower than in all other samples. For this reason, the Orion belt sample is likely not a robust representation of the brown dwarf period distribution at 3–5 Myr and should be treated with caution.

For further investigation, we compare with simple rotational evolution tracks overplotted in black lines. For stars, modelers typically use two simple contrasting cases to represent this phase from 1 to 10 Myr: constant angular momentum, i.e., spin-up due to contraction, versus constant period, i.e., "disk

locking" (Bouvier et al. 2014). To calculate tracks with constant angular momentum, we use radii from Baraffe et al. (2015) for a 0.05 $M_\odot$ brown dwarf, noting that exact choice of the mass or the track does not affect the outcomes in any significant way. The period is then $P = P_i (R/R_i)^2$. For the case of constant period, the track is simply $P = P_i$. In both cases, the index i indicates the initial value.

It is obvious from Figure 13 that the periods are not constant over time: the median period in UpSco, as well as the upper/lower limit, are significantly reduced compared to the periods in the ONC or Taurus. Comparing the period distributions in Taurus and Upper Sco, the median period drops by 46%, the 10th percentile by 36%, and the 90th percentile by 48%. Thus a track with constant period does not match the data. In dotted black lines, Figure 13 shows the case without angular momentum loss. The updated period samples for brown dwarfs do not fit this case either. Without any rotational braking the period is expected to drop by 70% of the initial period between the age of 1 and 8 Myr, substantially more than observed.

To achieve a better match, we construct a mixed track, where we keep the period constant for a specified time of period locking before starting the track with angular momentum conservation (solid black lines). This would correspond to a scenario where brown dwarfs experience rotational braking over a given timescale. With a locking timescale of 5 Myr, this model reproduces the broad parameters of the currently known period distributions. A more precise estimate of the locking timescale requires a better understanding of biases in the period distributions and ages of the objects with known periods. For example, if the Upper Sco brown dwarfs with known periods have ages of 5 Myr, as opposed to 8 Myr as assumed here, a shorter locking timescale of 3 Myr is more realistic. Be that as it may, there is clear evidence for rotational braking in young brown dwarfs from a comparison of periods in different regions. These new results supersede the earlier work on this subject by Scholz et al. (2015).

For comparison, modeling of the period evolution for low mass stars typically results in disk-locking timescales in the range of a few megayears, constrained from period samples that are significantly larger than those for brown dwarfs and include older objects as well. In Gallet & Bouvier (2015), the disk-locking timescale is found to be 2–9 Myr for 1 $M_\odot$, 3–5 Myr for 0.8 $M_\odot$, and 2.5–6 Myr for 0.5 $M_\odot$. This is not substantially different from the values inferred here for brown dwarfs. One main feature of the models for stars is that the locking timescale depends on the rotation itself, with fast rotators being locked for shorter timescales than slow rotators. So far, there does not seem to be any evidence for this trend in the brown dwarf samples.

Overall, the revised analysis of the rotational evolution with expanded samples reported here results in a major new finding: brown dwarf rotation is regulated over timescales of a few megayears, presumably by the presence of disks, similar to low mass stars.

7. Summary

In this paper we present a new analysis of rotation periods for brown dwarfs and very low mass stars in the Upper Scorpius young association. With an age of 5–10 Myr, this association is ideally suited to probe the early stages of rotational evolution in the very low mass regime, particularly the influence of the disks on rotation. We establish a period sample for 104 members of Upper Sco; depending on the assumed age, about a third of them should be brown dwarfs. With very few exceptions, the periods are all shorter than 3 days, with a median of 1.28 day, consistent with previous results. The median drops to 0.84 days for the subsample of likely brown dwarfs. Based on this sample, we present three main findings:

1. The rotational evolution of brown dwarfs from 1 to 10 Myr is inconsistent with angular momentum conservation, but can be explained by assuming a "locking" of the period for a few megayears, similar to previous findings for stars.
2. Objects with disks are predominantly slow rotators, with the median period among brown dwarfs with disks being about twice that for diskless objects.
3. For two brown dwarfs, there is direct evidence of disk-locking: their rotation period is comparable to the period of recurring dips in the light curve, most likely caused by warps in the inner disk.

Altogether, our findings constitute compelling evidence for regulation of rotation in brown dwarfs by disks. Previous studies were unable to establish such a link due to (a) the fast rotation of brown dwarfs (i.e., no clear gap between slow and fast rotators and no bimodal period distribution), (b) the limitations of ground-based monitoring, and (c) the limited sample size. Given that disk braking is clearly present in substellar objects, their fast rotation at young ages has to be a result of initial conditions, not early evolution. As discussed in Scholz et al. (2018), the rotation rates of very young brown dwarfs may provide clues about their origin.

Appendix

In the Appendix, we show phased light curves for all 104 periodic objects in our sample. These are plotted in the same order as displayed in Tables 1 and 2, and shown in Figures 14–20.
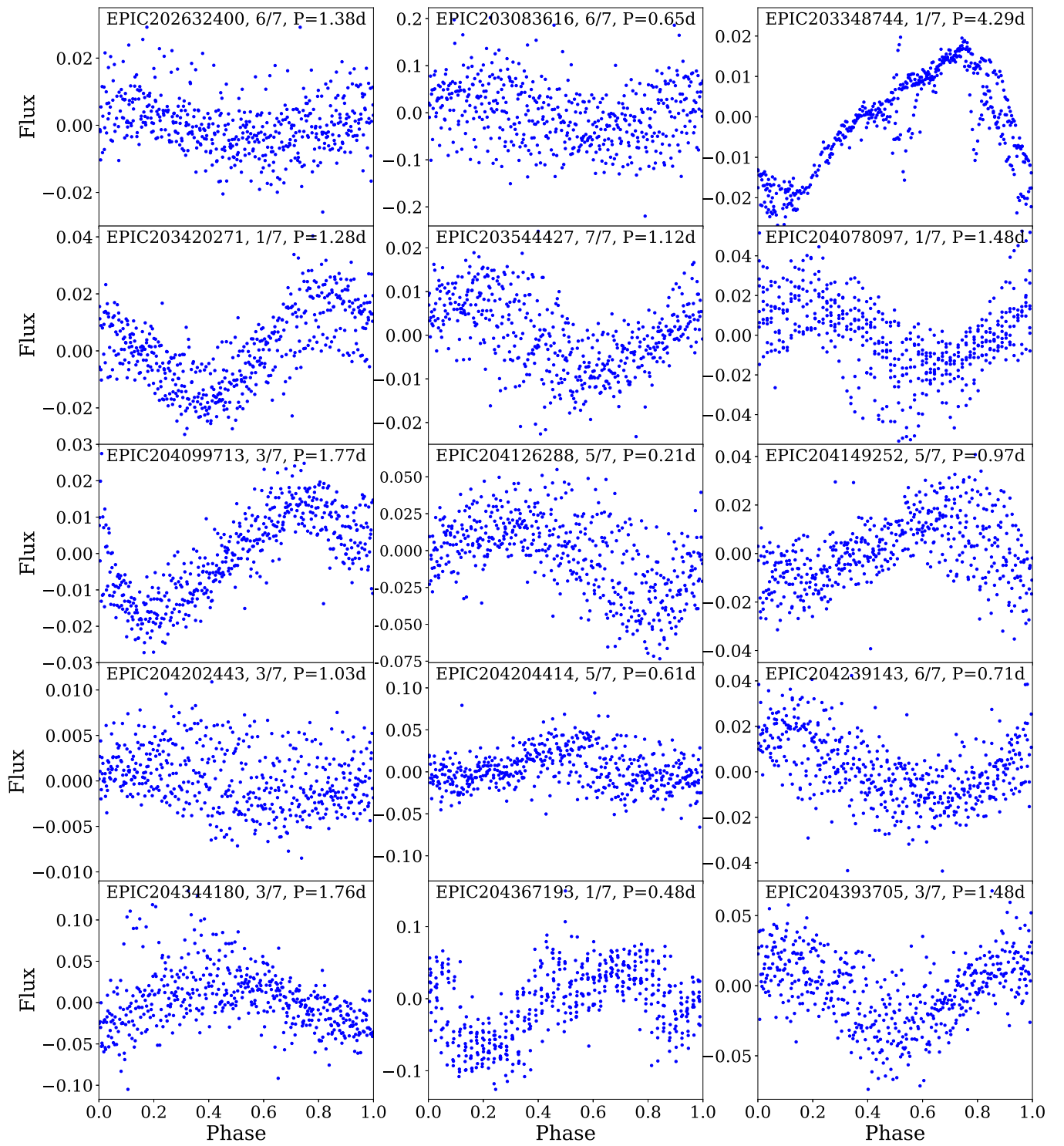
Figure 14. Phase plots of a light-curve segment, showing the flux change as a function of phase for the measured period, for the first 15 objects of Sample A.
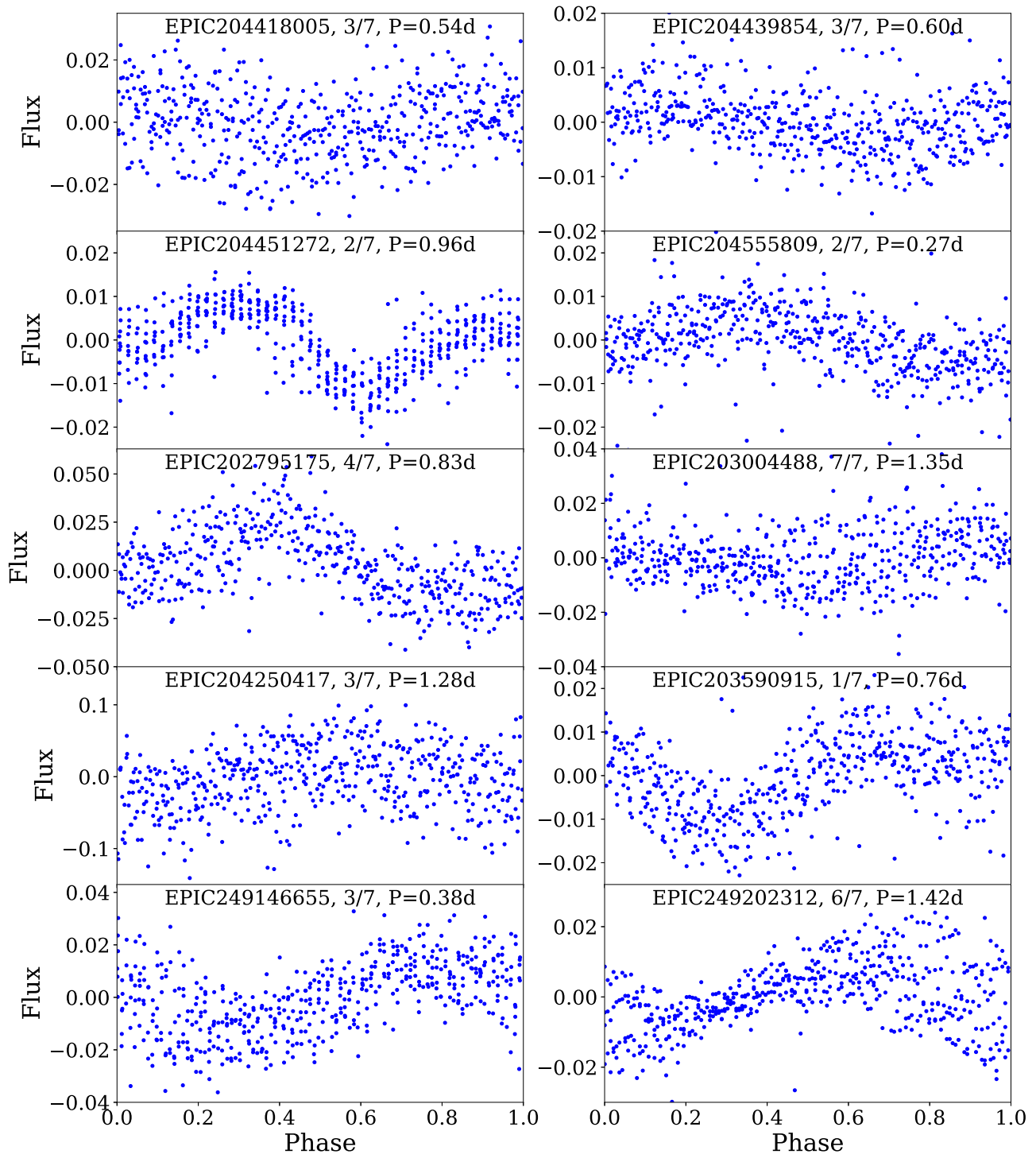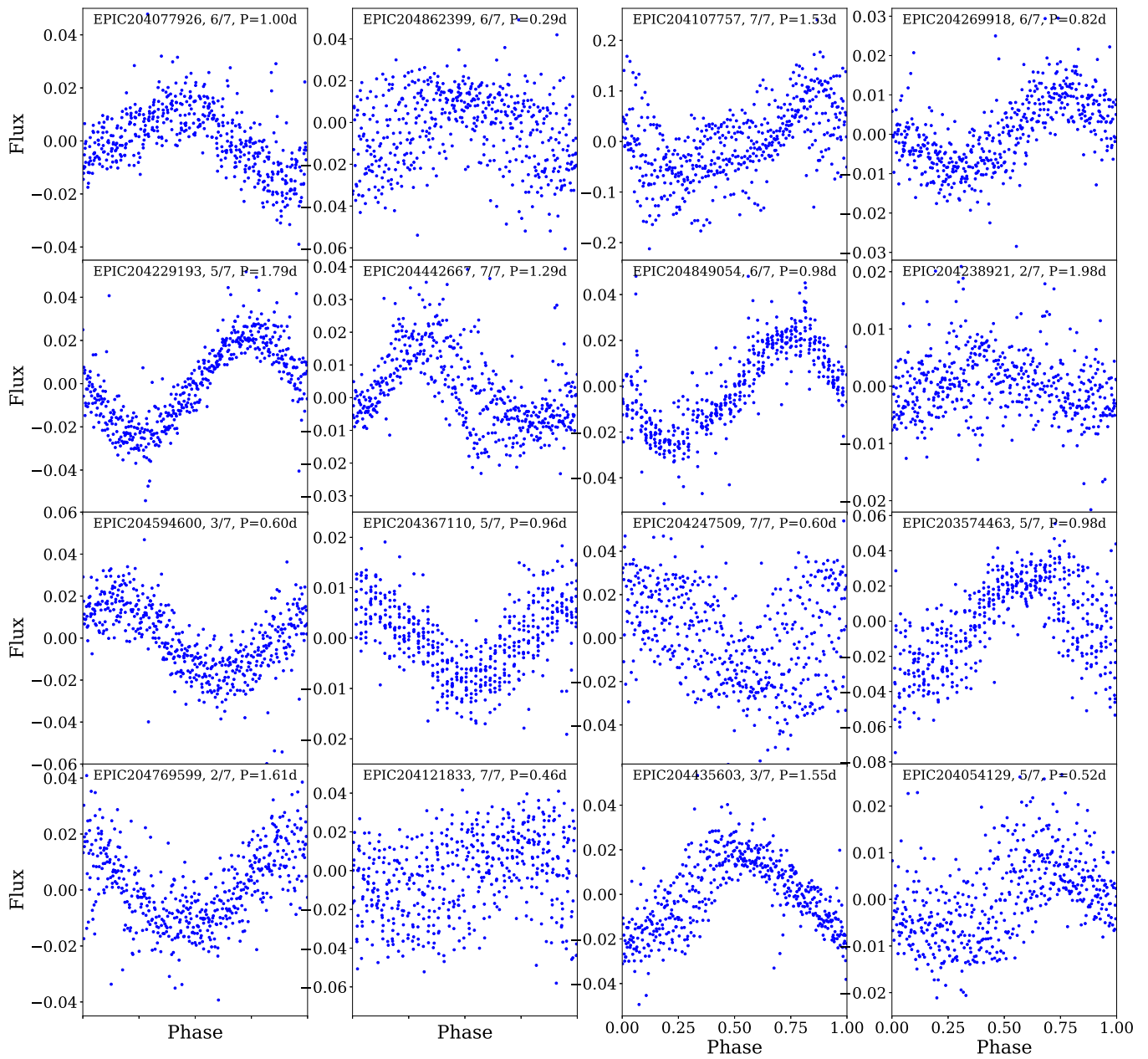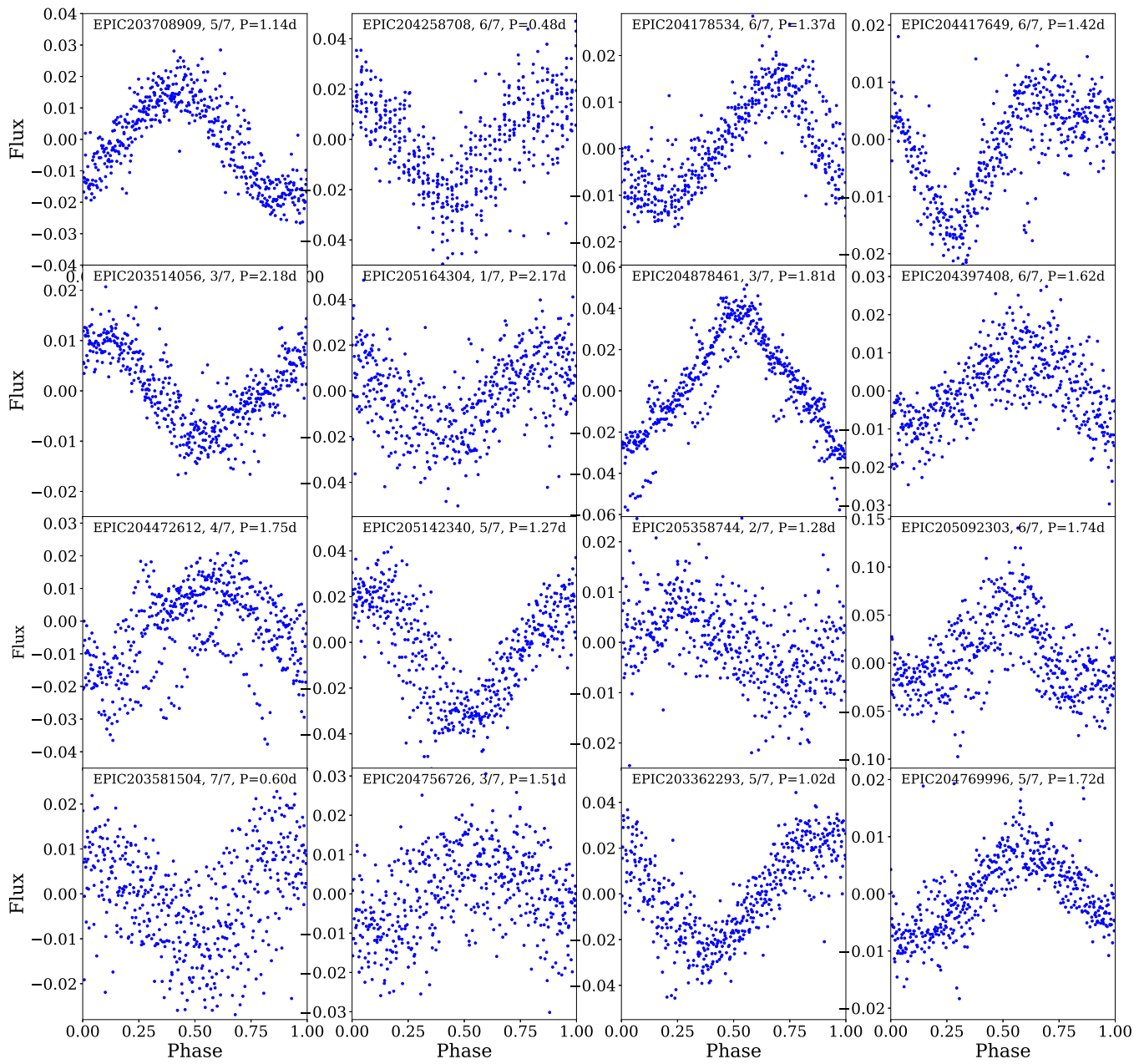
Figure 15. Same as Figure 14, but for the other 10 periodic objects of Sample A.
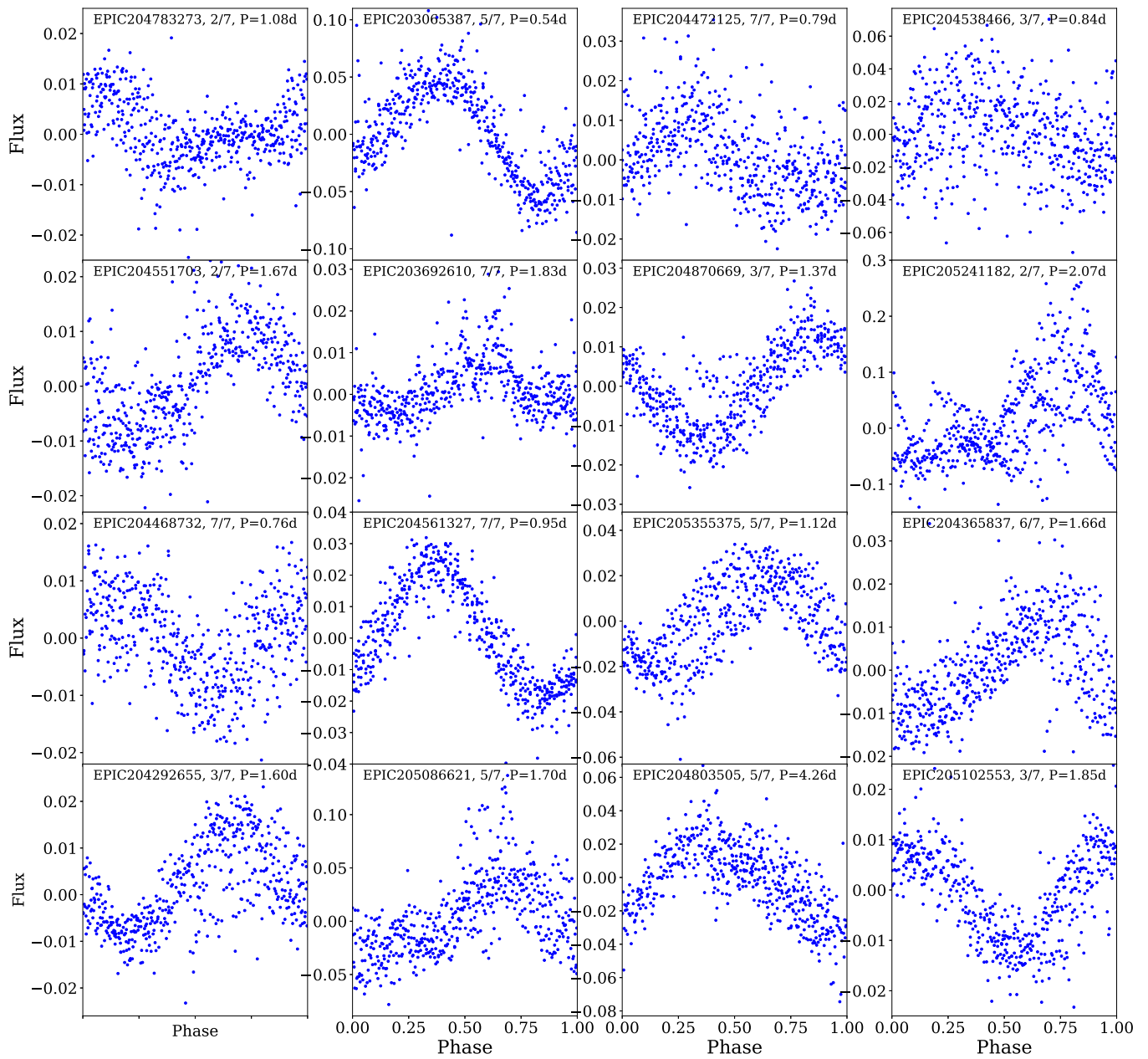
Figure 16. Phase plots of a light-curve segment, showing the flux change as a function of phase for the measured period, for the first 16 objects of Sample B.

Figure 17. Same as Figure 16, but for the second 16 periodic objects of Sample B.

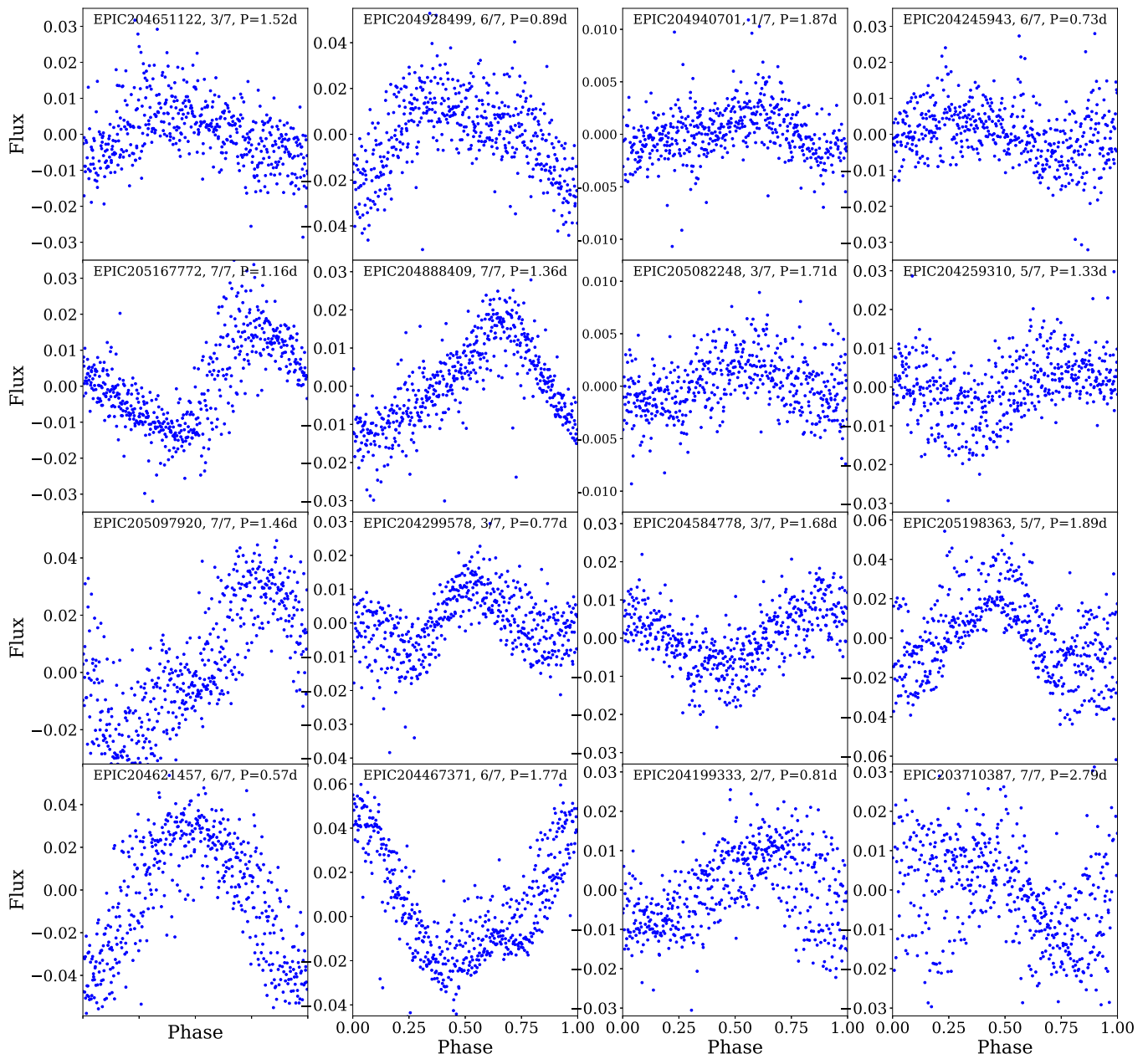**Figure 18.** Same as Figure 16, but for the third 16 periodic objects of Sample B.

Figure 19. Same as Figure 16, but for the fourth 16 periodic objects of Sample B.
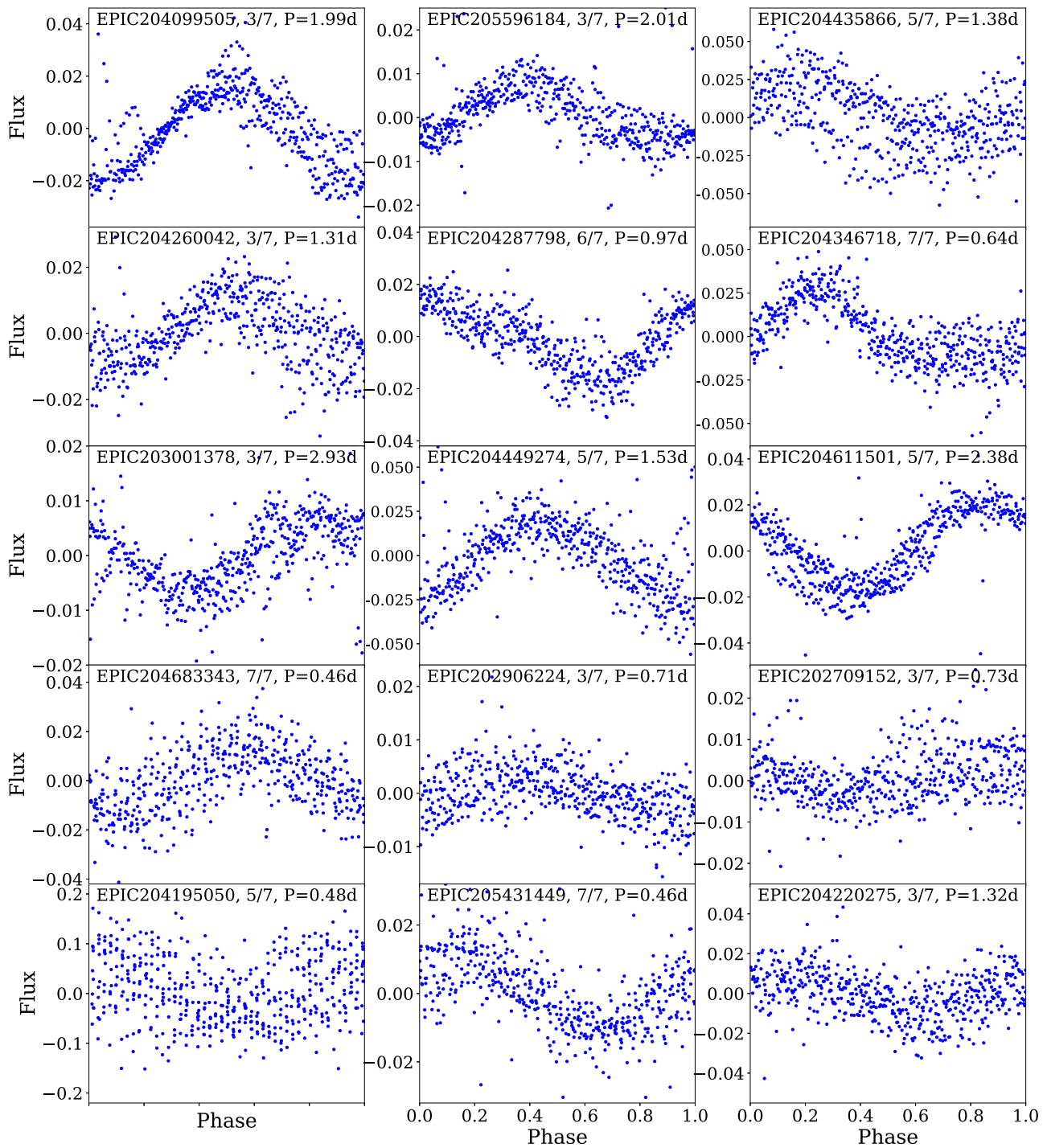
Figure 20. Same as Figure 16, but for the final 15 periodic objects of Sample B.

ORCID iDs

Aleks Scholz ⓘ https://orcid.org/0000-0001-8993-5053

References

Aigrain, S., Llama, J., Ceillier, T., et al. 2015, MNRAS, 450, 3211
Angus, R., Morton, T., Aigrain, S., Foreman-Mackey, D., & Rajpaul, V. 2018, MNRAS, 474, 2094
Ansdell, M., Gaidos, E., Rappaport, S. A., et al. 2016, ApJ, 816, 69
Astropy Collaboration, Robitaille, T. P., Tollerud, E. J., et al. 2013, A&A, 558, A33
Bailer-Jones, C. A. L., & Mundt, R. 2001, A&A, 367, 218
Baraffe, I., Homeier, D., Allard, F., & Chabrier, G. 2015, A&A, 577, A42
Bouvier, J., Matt, S. P., Mohanty, S., et al. 2014, in Protostars and Planets VI, ed. H. Beuther et al. (Tucson, AZ: Univ. of Arizona Press), 433
Bouy, H., & Martín, E. L. 2009, A&A, 504, 981
Bryan, M. L., Benneke, B., Knutson, H. A., Batygin, K., & Bowler, B. P. 2018, NatAs, 2, 138
Caballero, J. A., Béjar, V. J. S., Rebolo, R., & Zapatero Osorio, M. R. 2004, A&A, 424, 857
Cody, A. M., & Hillenbrand, L. A. 2010, ApJS, 191, 389
Cody, A. M., & Hillenbrand, L. A. 2014, ApJ, 796, 129
Cody, A. M., & Hillenbrand, L. A. 2018, arXiv:1802.06409
Cody, A. M., Hillenbrand, L. A., David, T. J., et al. 2017, ApJ, 836, 41
Cody, A. M., Stauffer, J., Baglin, A., et al. 2014, AJ, 147, 82
Cook, N. J., Scholz, A., & Jayawardhana, R. 2017, AJ, 154, 256
Cutri, R. M., Skrutskie, M. F., van Dyk, S., et al. 2003, yCat, 2246
Cutri, R. M., et al. 2013, yCat, 2328
Dawson, P., Scholz, A., Ray, T. P., et al. 2013, MNRAS, 429, 903
Dawson, P., Scholz, A., Ray, T. P., et al. 2014, MNRAS, 442, 1586
de Zeeuw, P. T., Hoogerwerf, R., de Bruijne, J. H. J., Brown, A. G. A., & Blaauw, A. 1999, AJ, 177, 354
Esselstein, R., Aigrain, S., Vanderburg, A., et al. 2018, ApJ, 859, 167
Gallet, F., & Bouvier, J. 2015, A&A, 577, A98
Giles, H. A. C., Collier Cameron, A., & Haywood, R. D. 2017, MNRAS, 472, 1618
Harding, L. K., Hallinan, G., Boyle, R. P., et al. 2013, ApJ, 779, 101
Hedges, C., Hodgkin, S., & Kennedy, G. 2018, MNRAS, 476, 2968
Herbst, W., Eislöffel, J., Mundt, R., & Scholz, A. 2007, in Protostars and Planets V, ed. B. Reipurth, D. Jewitt, & K. Keil (Tucson, AZ: Univ. of Arizona Press), 297
Howell, S. B., Sobeck, C., Haas, M., et al. 2014, PASP, 126, 398
Hunter, J. D. 2007, CSE, 9, 90
Joergens, V., Fernández, M., Carpenter, J. M., & Neuhäuser, R. 2003, ApJ, 594, 971
Jones, E., Oliphant, T., & Peterson, P. 2001, SciPy: Open Source Scientific Tools for Python, http://www.scipy.org
Kounkel, M., Covey, K., Suárez, G., et al. 2018, AJ, 156, 84
Lamm, M. H., Mundt, R., Bailer-Jones, C. A. L., & Herbst, W. 2005, A&A, 430, 1005
Lodieu, N., Dobbie, P. D., & Hambly, N. C. 2011, A&A, 527, A24
Luhman, K. L., & Mamajek, E. E. 2012, ApJ, 758, 31
McGinnis, P. T., Alencar, S. H. P., Guimarães, M. M., et al. 2015, A&A, 577, A11
McQuillan, A., Aigrain, S., & Mazeh, T. 2013, MNRAS, 432, 1203
McQuillan, A., Mazeh, T., & Aigrain, S. 2014, ApJS, 211, 24
Metchev, S. A., Heinze, A., Apai, D., et al. 2015, ApJ, 799, 154
Miles-Páez, P. A., Pallé, E., & Zapatero Osorio, M. R. 2017, MNRAS, 472, 2297
Mohanty, S., Jayawardhana, R., & Basri, G. 2005, ApJ, 626, 498
Paudel, R. R., Gizis, J. E., Mullan, D. J., et al. 2018, ApJ, 861, 76
Pecaut, M. J., & Mamajek, E. E. 2013, ApJS, 208, 9
Rebull, L. M., Stauffer, J. R., Cody, A. M., et al. 2018, AJ, 155, 196
Rebull, L. M., Stauffer, J. R., Megeath, S. T., Hora, J. L., & Hartmann, L. 2006, ApJ, 646, 297
Reiners, A., & Basri, G. 2008, ApJ, 684, 1390
Rodríguez-Ledesma, M. V., Mundt, R., & Eislöffel, J. 2009, A&A, 502, 883
Rodríguez-Ledesma, M. V., Mundt, R., & Eislöffel, J. 2010, A&A, 515, A13
Scholz, A. 2009, in AIP Conf. Proc. 1094 15th Cambridge Workshop on Cool Stars, Stellar Systems, and the Sun (Melville, NY: AIP), 61
Scholz, A., Brandeker, A., & Jayawardhana, R. 2005, ApJL, 629, L41
Scholz, A., & Eislöffel, J. 2004a, A&A, 419, 249
Scholz, A., & Eislöffel, J. 2004b, A&A, 421, 259
Scholz, A., & Eislöffel, J. 2005, A&A, 429, 1007
Scholz, A., Jayawardhana, R., Wood, K., et al. 2007, ApJ, 660, 1517
Scholz, A., Kostov, V., Jayawardhana, R., & Mužić, K. 2015, ApJL, 809, L29
Scholz, A., Moore, K., Jayawardhana, R., et al. 2018, ApJ, 859, 153
Schwarz, H., Ginski, C., de Kok, R. J., et al. 2016, A&A, 593, A74
Slesnick, C. L., Hillenbrand, L. A., & Carpenter, J. M. 2008, ApJ, 688, 377
Stauffer, J., Cody, A. M., Baglin, A., et al. 2014, AJ, 147, 83
Stauffer, J., Cody, A. M., McGinnis, P., et al. 2015, AJ, 149, 130
Stelzer, B., Damasso, M., Scholz, A., & Matt, S. P. 2016, MNRAS, 463, 1844
Van Der Walt, S., Colbert, S. C., & Varoquaux, G. 2011, arXiv:1102.1523
Vanderburg, A., & Johnson, J. A. 2014, PASP, 126, 948
Vasconcelos, M. J., & Bouvier, J. 2015, A&A, 578, A89
Vasconcelos, M. J., & Bouvier, J. 2017, A&A, 600, A116
Zapatero Osorio, M. R., Martín, E. L., Bouy, H., et al. 2006, ApJ, 647, 1405
Zhou, Y., Apai, D., Schneider, G. H., Marley, M. S., & Showman, A. P. 2016, ApJ, 818, 176